https://doi.org/10.5194/egusphere-2026-1878
Preprint. Discussion started: 26 June 2026


# Dynamical and Microphysical Interactions in a Coastal Bow-Echo Producing Extreme Rainfall

Jong-Hoon Jeong[1], Seung Hee Kim[2*], Su-Bin Oh[2], Jeong-Eun Lee[3], Chia-Lun Tsai[4], and Gyuwon Lee[3]

[1]Hoenywell Aerospace, Phoenix, Arizona, USA
[2]Institute for Earth, Computing, Human, and Observing (ECHO), Chapman University, Orange, California, USA
[3]BK21 Weather Extremes Education & Research Team, Department of Atmospheric Sciences, Center for Atmospheric Remote sensing (CARE), Kyungpook National University, Republic of Korea
[4]Department of Atmospheric Sciences, Chinese Culture University, Taipei, Taiwan

*Correspondence to*: Seung Hee Kim (sekim@chapman.edu)

**Abstract.** On 2 August 2020, a coastal bow-echo mesoscale convective system (MCS) produced severe rainfall and damaging winds over South Korea, resulting in casualties and property losses. Forecasting rapidly developing coastal bow echoes remains challenging due to limited understanding of the interactions between mesoscale dynamics and microphysical processes. Here, we analyze these interactions using improved multi-Doppler wind retrievals and polarimetric radar observations. The system evolved into a leading convective–trailing stratiform structure, reinforced by a rear-inflow jet (RIJ) that enhanced low-level convergence and shaped bowing segments. Feedbacks between RIJ-driven downdrafts, convective updrafts, and hydrometeor recycling sustained precipitation and prolonged the system's lifetime after landfall. In particular, mixed-phase hydrometeors in stratiform clouds were advected into the leading convective line, where they enhanced and maintained deep convection. These dynamic–microphysical interactions governed storm organization and rainfall efficiency, explaining the persistence of heavy precipitation in the coastal zone. Beyond advancing process understanding, our results highlight the role of land–sea contrasts in shaping mesoscale circulations that intensify convection and provide observational benchmarks for improving forecasts and hazard resilience in coastal regions.

## 1 Introduction

Mesoscale convective systems (MCSs) are among the dominant producers of warm-season precipitation in the tropics and midlatitudes, yet they remain a major source of forecast uncertainty because their internal organization and intensity can evolve rapidly. Within the MCS spectrum, bow echoes are particularly hazardous owing to their fast propagation, damaging surface winds, and potential to produce flash flooding and tornadoes (Coniglio et al., 2004; Fujita, 1987; Houze Jr., 2004; Przybylinski, 1995; Weisman, 1993). Bow echoes are readily identified by their arched radar-reflectivity signatures and recurved leading convective lines, which reflect the combined influence of convective updrafts, rear-inflow jets (RIJs), and mesoscale pressure gradients (Wakimoto, 2001; Weisman, 1992). Previous studies have shown that their evolution is governed by a dynamically

https://doi.org/10.5194/egusphere-2026-1878
Preprint. Discussion started: 26 June 2026


balanced interaction between the cold pool and the ambient vertical wind shear, which controls the maintenance of the leading convective line, the development of RIJs, and the formation of mesoscale vortices along the bow apex and bookend regions (Adams-Selin et al., 2013; Parker and Johnson, 2000; Rotunno et al., 1988). These dynamical interactions are not merely diagnostic features; they strongly regulate surface-wind production, convective regeneration, and overall longevity of the system (Cifelli et al., 2002; Morrison et al., 2009; Wakimoto, 2001).

While the dynamical framework of bow echoes has been documented in considerable detail, the microphysical processes that modulate their evolution and rainfall production remain less well constrained. Processes such as collision–coalescence, riming, melting, and evaporation alter latent-heating distributions and hydrometeor loading, thereby influencing buoyancy, downdraft strength, and precipitation efficiency (Cifelli et al., 2002; Heymsfield et al., 2009; Morrison et al., 2009). In bow echoes, these effects differ substantially between convective and stratiform cloud regions, where contrasting heating and cooling profiles can either reinforce or weaken system-scale circulations (Braun and Houze, 1997; Houze, 1989, 1997). This coupling may be especially important because RIJs can redistribute ice and liquid hydrometeors from the trailing stratiform cloud region toward the leading convective line, potentially promoting new cell growth and prolonging storm organization (Bryan and Morrison, 2012; Tao et al., 2012). However, direct observational evidence linking storm-scale airflow, hydrometeor evolution, and rainfall enhancement in bow echoes remains limited. As a result, a key outstanding question is how mesoscale dynamics and cloud microphysics interact to sustain bow-echo structure and heavy precipitation.

This question is particularly important in coastal regions of East and Southeast Asia, where bow echoes occur frequently and often produce societally significant impacts due to the high population density of coastal urban areas. In these regions, convective systems commonly evolve in an environmental shaped by strong land-sea thermal contrasts, complex coastlines, steep terrain, and abundant low-level moisture supplied by monsoonal flow or nearby tropical cyclones (Jeong et al., 2016; Kang et al., 2018; Liu et al., 2018). Such conditions favor the development and maintenance of organized convection near the coastline and can enhance low-level convergence, convective instability, and moisture transport before and after landfall. Bow echoes in these settings are therefore not only wind-producing systems but also efficient heavy-rainfall producer, especially when their propagation slows or when coastal forcing helps repeatedly regenerate convection. Despite their frequency and impact, the processes through which coastal boundary effects modify the internal dynamic and microphysical structure of bow echoes remain poorly understood.

Addressing this problem requires observations capable of resolving both the airflow structure and the evolving precipitation particles within storms. Although East Asia is equipped with extensive Doppler-radar networks, obtaining such observations remains challenging in coastal environments. Offshore dual-Doppler overlap is often limited, mountainous terrain can partially block radar beams, and the rapidly translational speed of MCSs reduces the duration over which high-quality, coincident observations can be collected. These observational constraints have led many previous studies in the region to focus primarily on climatological characteristics, environmental conditions, or synoptic-scale precursors, rather than on the storm-scale processes that directly control bow-echo maintenance and rainfall production (Chen et al., 2019, 2022; Cui et al., 2021).

https://doi.org/10.5194/egusphere-2026-1878
Preprint. Discussion started: 26 June 2026


Consequently, the dynamic-microphysical feedbacks operating within coastal bow echoes remain under-observed and insufficiently quantified.

Recent advances in radar-based remote sensing now provide an opportunity to address this gap more directly. Dual-polarization radar offers information on hydrometeor type, shape, orientation, and phase transition through polarimetric variables, enabling detailed inference of precipitation microphysics (Kumjian et al., 2022; Ryzhkov and Zrnic, 1998). Multi-Doppler radar synthesis, in turn, reconstructs the three-dimensional wind field by combining radial-velocity measurements from multiple radars, allowing diagnosis of RIJs, convergence zones, vertical motions, and embedded circulations (Gao et al., 1999; Ray et al., 1980). When combined, these techniques enable simultaneous analysis of kinematic structure and microphysical evolution of convective systems within a physically consistent framework. Such an integrated perspective is essential for understanding how airflow redistributes hydrometeors, how latent-heating patterns feed back on storm dynamics, and how these coupled processes regulate convective organization and precipitation efficiency.

In this study, we apply these complementary observational approaches to a bow-echo MCS that affected the west coast of South Korea on 2 August 2020 and produced 235 mm of rainfall along with damaging surface winds. This event provides a rare opportunity to examine, from observations alone, how mesoscale dynamics, microphysical evolution, and coastal boundary influences interact within a landfalling bow echo. We integrate multi-Doppler wind retrievals with polarimetric radar analyses to construct a unified depiction of the storm's structural evolution and to identify the mechanisms through which hydrometeors advected from the stratiform region contributed to sustaining the leading convective line. The objectives of this study are to: (1) characterize the synoptic and mesoscale environments that favored bow-echo formation in a coastal setting; (2) diagnose the three-dimensional wind and circulation structures, including the RIJ and embedded vortices; (3) quantify microphysical variability between convective and stratiform cloud regions using polarimetric radar measurements; and (4) examine how dynamic-microphysical coupling influenced storm organization and precipitation efficiency during and after landfall.

The remainder of this paper is organized as follows. Section 2 describes the radar datasets and analysis methods, including multi-Doppler synthesis, polarimetric radar retrievals, and echo classification. Section 3 presents the synoptic environment and the observed dynamic-microphysical interactions. Section 4 summarizes the main findings and discusses their broader implications for understanding coastal bow echoes and associated heavy-rainfall hazards.

## 2 Data and Methodology

This study investigates the dynamical and microphysical characteristics of a bow-echo MCS using multiple observational datasets. The primary datasets include dual-polarization radar observations from the Korea Meteorological Administration (KMA) and the Ministry of Environment (ME) network, upper-air soundings, and surface measurements from the Automated Synoptic Observing System (ASOS) and Automatic Weather Stations (AWS). These observations are complemented by ERA5

https://doi.org/10.5194/egusphere-2026-1878
Preprint. Discussion started: 26 June 2026


reanalysis data (Hersbach et al., 2020), with 0.25° spatial resolution and hourly output, to characterize the large-scale dynamical environment and moisture transport.

### 2.1 Three-Dimensional Wind Retrieval from Multiple-Doppler Radar Analysis

To examine the dynamical structure of the bow-echo system, we retrieved three-dimensional wind fields using multiple dual-polarization Doppler radars. The radar network consists of five X-band radars (XMIL, XJDK, XSRI, XKOU, and YKOU), two C-band radars (CIIA and CSAN), and four S-band radars (SGDK, SKWK, SBRI, and SKSN) operated by KMA and ME. The radar locations are shown in Fig. 1 and Table 1.

Prior to wind retrieval, radar data were subjected to quality control to remove non-meteorological echoes using a fuzzy logic algorithm (Cho et al., 2006; Ye et al., 2015). Radar volumes with more than 10% beam blockage by terrain were excluded to ensure data quality. Three-dimensional wind fields were then derived using the Wind Synthesis System using Doppler Measurements (WISSDOM; Liou and Chang, 2009; Tsai et al., 2023). The WISSDOM employs a variational framework that minimizes a cost function subject to multiple physical and observational constraints. Although originally developed for flat terrain, the system was later extended to complex terrain using an immersed boundary method (IBM; Liou et al. 2012). The IBM introduces ghost cells near terrain boundaries, allowing improved interpolation and reconstruction of flow fields in regions with complex topography. This capability is particularly important over the Korean Peninsula, where orography strongly influences low-level flow during convective events.

The original WISSDOM formulation minimizes a cost function that includes five constraints: (1) radar radial velocity and reflectivity observations, (2) a background wind field, (3) mass continuity, (4) vorticity conservation, and (5) spatial smoothness (Laplacian constraint). In this study, we employ a modified version of WISSDOM (Tsai et al., 2023) that incorporates three additional constraints to improve retrieval accuracy. These additional terms penalize discrepancies between retrieved winds and independent observations, including radiosonde soundings, surface wind measurements, and local reanalysis fields. This extension enhances retrieval performance, particularly in regions with sparse radar coverage or complex terrain.

The background wind field was constructed using radiosonde observations, AWS measurements, and output from the Local Data Assimilation and Prediction System (LDAPS) provided by KMA. The locations of the radiosonde (black square) and AWS sites (red circles) are shown in Fig. 1. The wind synthesis was performed on a Cartesian grid with 500 m horizontal and 250 m vertical resolution over a domain of 300 × 300 km², extending up to 10 km in height and centered on the mature stage of the bow echo (Fig. 1b).

https://doi.org/10.5194/egusphere-2026-1878
Preprint. Discussion started: 26 June 2026


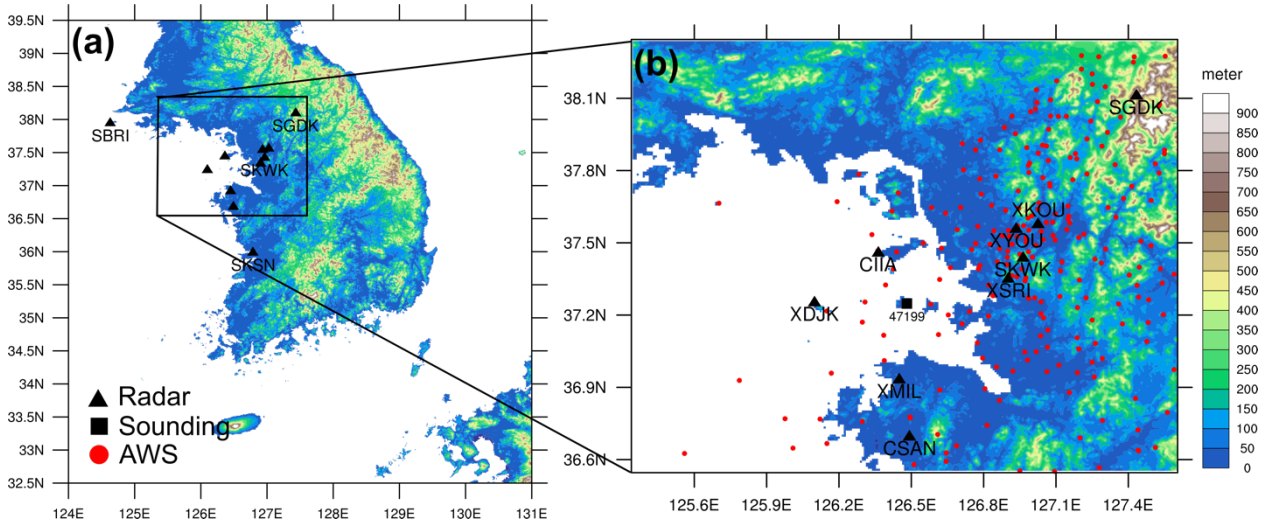


**Figure 1: Locations of radars, sounding, and Automatic Weather Station (AWS) sites at (a) the entire South Korea and (b) the WISSDOM domain. A black triangle denotes the locations of the radar, a black square denotes the location of the sounding (47199), and red triangles mark the AWS sites. Topography features are indicated by color shading.**

### 2.2 Radar Microphysical Retrievals

To examine microphysical processes within the bow-echo MCS, we used observations from the KMA S-band polarimetric radar network. These radars provide measurements of horizontal reflectivity ($Z_H$), differential reflectivity ($Z_{DR}$), correlation coefficient ($\rho_{HV}$), and differential phase ($\Phi_{DP}$), with a range resolution of 250 m and an azimuthal resolution of 1.0°. Volume scans with 10 elevation angles were conducted every 5 minutes, enabling detailed analysis of storm evolution.

Key retrieved microphysical parameters include liquid water content (LWC), ice water content (IWC), median volume diameter (Dm), and total number concentration (Nt). These quantities are estimated using empirical relationships based on polarimetric variables, particularly $Z_H$, $Z_{DR}$, and specific differential phase ($K_{DP}$).

For liquid-phase retrievals, we apply the following empirical relations derived from disdrometer observations (Brandes et al., 2004):

$$LWC = 1.38 \times 10^{-3} \times 10^{(0.1Z - 2.43Z_{DR} + 1.12Z_{DR}^2 - 0.176Z_{DR}^3)}, \quad (1)$$

$$\log(N_t) = -2.37 + 0.1Z - 2.89Z_{DR} - 1.28Z_{DR}^2 - 0.213Z_{DR}^3, \quad (2)$$

where LWC is in g m$^{-3}$, and Nt is in L$^{-1}$.

For ice-phase retrievals, two sets of equations are applied depending on the reliability of $Z_{DR}$. When $Z_{DR}$ is reliable, we use:

$$IWC\ (K_{DP}, Z_{DR}) = 4.0 \times 10^{-3} \left(\frac{K_{DP}\lambda}{1 - Z_{dr}^{-1}}, \right), \quad (3)$$

$$D_m\ (K_{DP}, Z_{DP}) = -0.1 + 2.0 \left(\frac{Z_{DP}}{K_{DP}\lambda}\right)^{0.5}, \quad (4)$$

where λ is the radar wavelength (mm), $Z_{DR} = 10^{0.1Z_{DR}}$, and $Z_{DP} = Z(1 - Z_{DR}^{-1})$, with $Z_H$ expressed in linear units (mm$^6$ m$^{-3}$).

When $Z_{DR}$ is small ($Z_{DR}$ < 0.4 dB; Carlin et al., 2021), alternative relationships are used

https://doi.org/10.5194/egusphere-2026-1878
Preprint. Discussion started: 26 June 2026


$$IWC = 3.3 \times 10^{-2}(K_{DP}\lambda)^{0.67}Z^{0.33}, \quad (5)$$

$$D_m = 0.67\left(\frac{Z}{K_{DP}\lambda}\right)^{1/3}, \quad (6)$$

The $K_{DP}$–$Z_{DR}$-based relations are less sensitive to particle orientation but require accurate $Z_{DR}$ measurements. In contrast, the $Z_{DR}$-independent relations are more robust under low-$Z_{DR}$ conditions but rely more strongly on assumptions about particle density and scattering properties. The combined use of these methods allows flexible and condition-dependent retrieval of microphysical properties.

### 2.3 Classification of Convective and Stratiform Regions

To examine interactions between trailing stratiform clouds and the leading convective line, we applied an objective echo classification method to distinguish convective and stratiform regions.

Convective regions are characterized by strong horizontal variability and vertically coherent reflectivity cores, whereas stratiform regions are more horizontally uniform and often exhibit a bright band near the melting layer. Numerous classification methods have been developed based on these structural differences (Houze, 1973; Churchill and Houze, 1984; Steiner et al., 1995; Yuter and Houze, 1997; Biggerstaff and Listemaa, 2000). However, traditional approaches often struggle to identify shallow convection embedded within stratiform regions, particularly when reflectivity values fall below standard thresholds (Powell et al., 2016). Additional challenges arise during transitions between shallow and deep convection.

To address these limitations, Powell et al. (2016) proposed a refined classification scheme that includes six categories: convective, stratiform, weak echo, isolated convective core, isolated convective fringe, and uncertain. This framework improves the representation of complex echo structures and reduces classification ambiguity.

In this study, we adopt the Powell et al. (2016) method but retain only the convective and stratiform categories for analysis. Intermediate categories are used during preprocessing to improve classification accuracy but are subsequently grouped into either convective or stratiform classes.

Figure 2 shows an example of echo classification during the landfall of the bow-echo system. The method successfully identifies the bow-shaped leading convective line and the trailing stratiform region. Weak echoes embedded within stratiform regions, as well as isolated convective features ahead of and behind the main system, are also effectively captured.

https://doi.org/10.5194/egusphere-2026-1878
Preprint. Discussion started: 26 June 2026


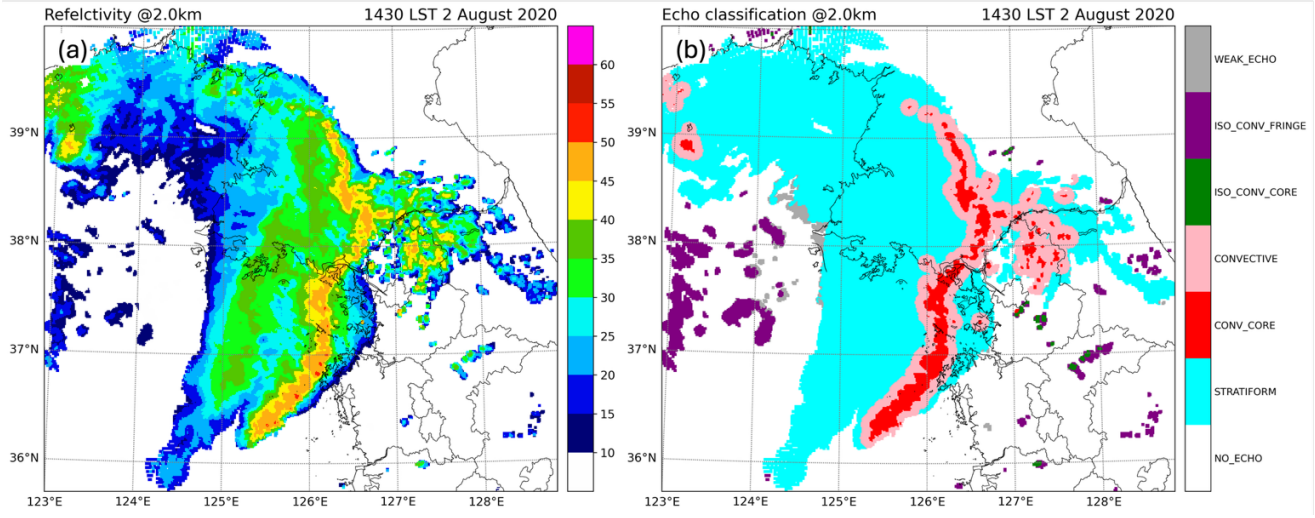


**Figure 2: (a) Radar reflectivity (dBZ, shading) and (b) echo classifications at an altitude of 2 km at 1430 LST 2 August 2020. Colors indicate stratiform (cyan), convective core (red), convective (pink), isolated convective core (green), isolated convective fringe (purple), and weak echo (gray).**

## 3 Results

### 3.1 Synoptic environment

The synoptic-scale environment on 2 August 2020 was highly favorable for the development and maintenance of the bow-echo MCS over the Korean Peninsula. ERA5 reanalysis at 0900 LST showed a relatively strong surface pressure gradient of approximately 1.1 hPa per 100 km between a surface low-pressure system and the North Pacific Subtropical High (NPSH) (Fig. 3a). This pressure gradient supported strong southwesterly low-level flow from lower latitudes. The flow was further enhanced by confluence between the cyclonic circulation associated with the deepening surface low and the anticyclonic circulation along the western periphery of the NPSH. As a result, the large-scale environment favored persistent transport of warm, moist air toward the Korean Peninsula.

At 850 hPa (Fig. 3b), southwesterly winds reached approximately 15 m s-1, exceeding the 12.5 m s-1 threshold commonly used to define a low-level jet (LLJ) in East Asia (Chen and Yu, 1988). This LLJ was collocated with elevated equivalent potential temperature ($\theta$e), indicating strong warm- and moist-air advection into the lower troposphere. Such a configuration is favorable for convective initiation and maintenance because it continuously replenishes the low-level inflow with high-$\theta$e air, thereby sustaining buoyancy and promoting deep convection. In addition, the persistent southwesterly flow likely enhanced moisture convergence along the west coast of Korea, where the convective system later intensified during landfall.

The synoptic environment was also influenced by two tropical cyclones: Typhoon Hagupit over the East China Sea and Typhoon Sinlaku near Vietnam (Fig. 3a). Although neither storm directly affected the Korean Peninsula, their broader

https://doi.org/10.5194/egusphere-2026-1878
Preprint. Discussion started: 26 June 2026


circulation likely contributed to enhanced poleward moisture transport. This large-scale moisture configuration resembles a predecessor rain event (PRE), in which heavy rainfall develops well poleward of a tropical cyclone in association with sustained transport of tropical moisture. In the present case, the combination of tropical moisture transport, strong low-level southwesterlies, and high $\theta e$ likely preconditioned the environment for organized deep convection and heavy rainfall.

At 500 hPa, a synoptic-scale trough was located near 120°E and exhibited a northwestward tilt (Fig. 3c). Ahead of this trough, strong southwesterly flow exceeding 30 m s-1 was present over the western part of the Korean Peninsula, indicating a dynamically active midtropospheric environment favorable for ascent. At 300 hPa, an upper-level jet (ULJ) streak was positioned between 39 and 43°N near the base of the trough, with wind speeds of 25–35 m s-1 (Fig. 3d). The Korean Peninsula was located near the jet-exit region, where directional diffluence likely enhanced upper-level divergence. The superposition of upper-level dynamical forcing, strong low-level moisture transport, and thermodynamic instability created a vertically coupled environment highly conducive to sustained, organized convection (Uccellini and Johnson, 1979). Thus, the bow-echo MCS developed within a synoptic setting characterized by strong lower-tropospheric forcing, abundant moisture supply, and favorable upper-level support for ascent.

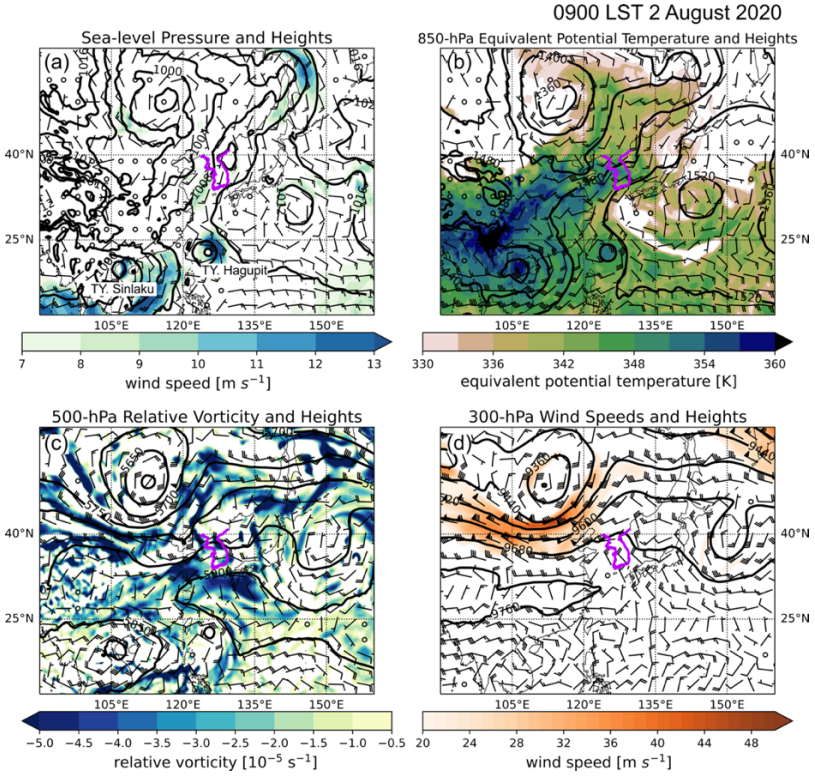


**Figure 3: Synoptic conditions at 0900 LST on 2 August 2020: (a) 10 m winds (m s$^{-1}$, barbs and shading) and mean sea-level pressure (hPa, contours every 4 hPa), (b) equivalent potential temperature (K, shading), horizontal winds (barbs), and geopotential height (gpm, contours every 40 gpm) at 850 hPa, (c) relative vorticity (10$^{-5}$ s$^{-1}$, shading), horizontal winds (barbs), and geopotential height**

https://doi.org/10.5194/egusphere-2026-1878
Preprint. Discussion started: 26 June 2026


**(gpm, contours every 50 gpm) at 500 hPa, and (d) wind speed (m $s^{-1}$, shading), horizontal winds (barbs), and geopotential height (gpm, contours every 80 gpm) at 300 hPa. The thick purple line indicates the Korean Peninsula.**

### 3.3 Kinematic structure of the bow-echo MCS

Before analyzing the detailed wind structure of the bow echo, we first identified the main life-cycle stages of the convective system using a quasi-objective approach. Specifically, we examined time series of the mean height of reflectivity exceeding 40 dBZ, used here as a proxy for convective depth, together with the 15 dBZ echo-top height in the convective and stratiform regions identified by the echo classification method. The mature stage was defined as the period during which both measures remained relatively stable, whereas a subsequent decrease in both quantities marked the transition to the decay stage.

Figure 4a shows the temporal evolution of the convective height and echo-top height from 1200 to 1700 LST on 2 August 2020. During the mature stage, both quantities remained relatively steady, with a mean convective height of 4.7 km and a mean echo-top height of 7.7 km. After 1600 LST, both values decreased noticeably, with the convective height falling to 4.4 km and the echo-top height to 7.2 km, indicating the onset of the decay phase. We also examined the time evolution of convective and stratiform areal coverage (Fig. 4b). During the mature stage, particularly after 1300 LST, the convective area gradually decreased as the system moved farther inland, whereas the stratiform area continued to expand and remained extensive even into the early decay phase. This evolution suggests that, although the leading convective line began to weaken gradually after landfall, the trailing stratiform region remained dynamically and microphysically active. The period from 1400 to 1430 LST therefore represents a particularly important stage, when the bow echo was mature and the contrast between the leading convective and trailing stratiform regions was most clearly defined.

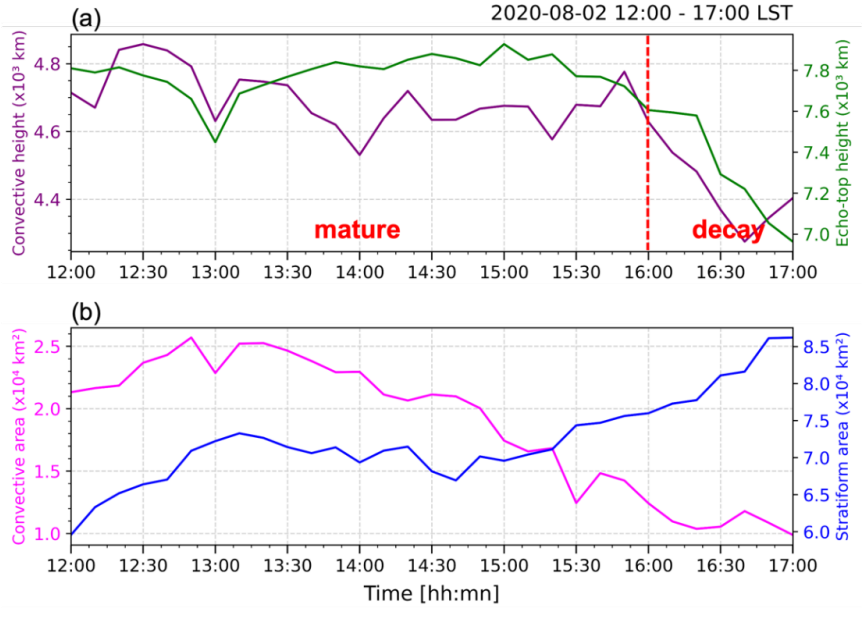


**Figure 4: Time series of (a) convective height (reflectivity Z > 40 dBZ; purple line) and echo-top height (Z = 15 dBZ; green line), and (b) convective area (pink line) and stratiform area (blue line) derived from the echo classification method. The red dashed line denotes the subjectively determined transition from the mature to decay stage.**

https://doi.org/10.5194/egusphere-2026-1878
Preprint. Discussion started: 26 June 2026


The horizontal radar reflectivity field during the mature stage reveals the structural evolution of the system into a classic leading-convective-line and trailing-stratiform (LCTS) configuration (Fig. 5). At 1330 LST, as the system approached the coast, it consisted of a narrow and intense leading convective line followed by a broad region of weaker stratiform precipitation (Fig. 5a), consistent with previously documented LCTS archetypes (Houze, 2018; Smull and Houze, 1985). This structure indicates that the system had already developed a well-organized mesoscale circulation, with active convective generation at the leading edge and widespread hydrometeor growth, advection, and fallout in the trailing region.

As the system neared the coastline, the leading convective line evolved into a more distinct bow-shaped structure (Fig. 5b). Two bowing segments became evident, oriented approximately southeast to northwest, and the southern segment exhibited a more pronounced RIJ in the multiple-Doppler wind retrievals. At 2 km altitude, system-relative southwesterly RIJ winds reached about 13 m $s^{-1}$. Although this magnitude is slightly weaker than the >15 m $s^{-1}$ values reported in some previous bow-echo studies (Meng et al., 2012; Smull and Houze, 1985; Weisman, 1993), it is still dynamically significant because descending rear inflow can efficiently transport horizontal momentum toward the surface and help intensify near-surface winds. In addition, the strengthening RIJ likely contributed to the forward acceleration and increasing curvature of the convective line.

By 1430 LST (Fig. 5c), the system had developed into a well-defined bow echo, and the RIJ intensified to nearly 15 m $s^{-1}$. At this stage, the bow apex became more pronounced and the leading line exhibited stronger curvature, consistent with the role of RIJ intensification in amplifying the bowing structure. The system also displayed a clear asymmetry in its mesovortex structure. Whereas idealized bow echoes often show paired cyclonic and anticyclonic bookend vortices of comparable strength, this case was dominated by a broader and stronger anticyclonic circulation on the northern flank, while the southern cyclonic circulation was weaker and more confined. This asymmetric circulation likely contributed to the uneven deformation of the line and may also have affected the local distribution of convergence and rear inflow along the bow.

After landfall, at 1500 LST (Fig. 5d), the RIJ remained evident and the convective line retained its bow-shaped morphology, indicating that the system remained dynamically organized even as it began to weaken. However, the forward propagation speed decreased to approximately 28 m $s^{-1}$, likely due in part to increased surface friction over land and weakening low-level inflow. Despite this deceleration, the leading convective line remained coherent, suggesting that the storm retained sufficient mesoscale organization to sustain deep convection for some time after landfall.

Additional insight into the storm-scale dynamics is provided by the divergence field at 2 km altitude derived from the multiple-Doppler synthesis (Fig. S2). The leading convective line was collocated with a zone of strong low-level convergence, as expected for sustained convective updrafts. Convergence became especially focused along the central part of the line near the coast, where onshore and offshore flows interacted. This spatial pattern suggests that coastal boundary effects, including land-sea contrasts and frictional convergence, may have locally enhanced inflow into the convective line during landfall. The divergence field also highlights the embedded mesoscale circulations associated with the bow echo. In the northern part of the system, the anticyclonic circulation was accompanied by divergence south of its center and convergence north of it, whereas the southern flank contained a weaker cyclonic circulation. Together, these features indicate that the bow echo was maintained by a strongly organized mesoscale flow field rather than by isolated convective cells alone.

https://doi.org/10.5194/egusphere-2026-1878
Preprint. Discussion started: 26 June 2026


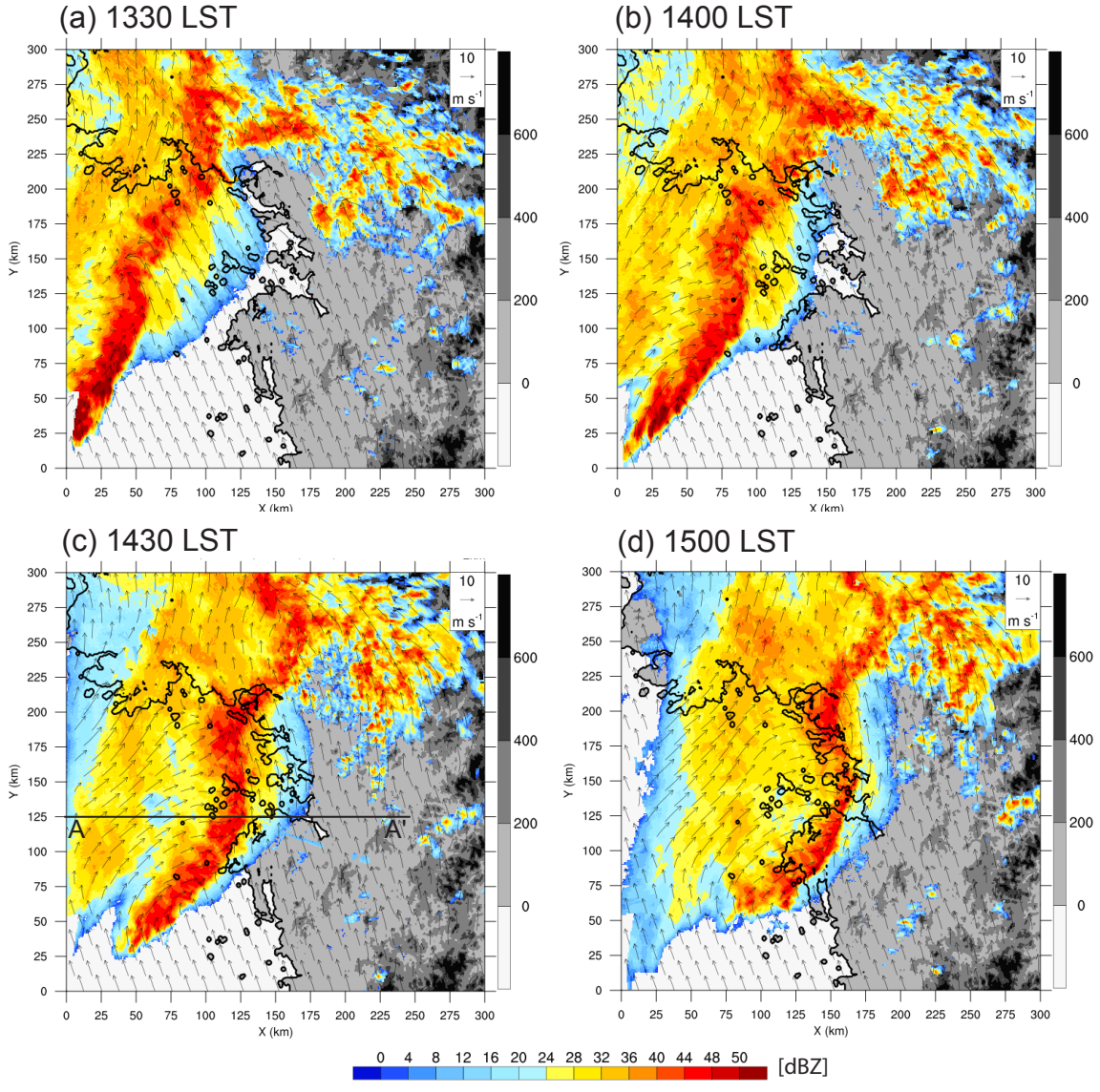


**Figure 5: Radar reflectivity (dBZ; shading) and system-relative winds (m s$^{-1}$; vectors) at 2 km altitude on 2 August 2020 at (a) 1330, (b) 1400, (c) 1430, and (d) 1500 LST. The black solid line in (c) indicates the location of the vertical cross section shown in Fig. 6. The reference wind vector is shown in the upper right.**

To better understand the vertical structure of the bow echo, we examined a cross section along transect A–A′ (X = 0–250 km, Y = 125 km) (Fig. 6). The cross sections clearly show the principal components of the LCTS system. At the leading edge, reflectivity greater than 35 dBZ extended upward to approximately 8 km and was collocated with a strong convective updraft exceeding 5 m s$^{-1}$ (Fig. 6a). A bounded weak echo region (BWER) was also evident between X = 60 and 90 km as a local minimum in reflectivity enclosed by stronger echoes. The BWER is indicative of a strong updraft that rapidly lofted hydrometeors, limiting their residence time in the lower portion of the radar volume and thereby reducing local reflectivity.

https://doi.org/10.5194/egusphere-2026-1878
Preprint. Discussion started: 26 June 2026


As the system progressed inland (Fig. 6b), the trailing stratiform region became increasingly prominent in the vertical cross section. By 1430 LST (Fig. 6c), the bow echo exhibited a mature vertical structure characterized by a strong leading convective updraft, descending rear inflow behind the line, and an extensive trailing stratiform cloud. At 1500 LST (Fig. 6d), the system weakened somewhat in vertical extent and reflectivity, but the leading line still maintained reflectivity exceeding 40 dBZ, indicating that deep convection persisted even after landfall.

The vertical wind field further clarifies the dynamical coupling between the convective and stratiform regions. Behind the leading line, descending midlevel flow associated with the RIJ was embedded within the stratiform cloud. This rear inflow likely strengthened the mesoscale downdraft and supported the maintenance of the trailing stratiform region. At the same time, warm, moist low-level inflow ascended along the leading edge of the system, sustaining the convective updraft. The juxtaposition of strong ascending flow at the front and descending rear inflow aloft is consistent with the canonical airflow structure of mature bow echoes and helps explain how the system maintained both a strong leading convective line and a broad trailing stratiform shield.

A recirculation-like airflow pattern was also evident between the convective core and the stratiform region, especially around X = 50–90 km in Fig. 6c. In this area, hydrometeors lofted within the leading convective line appear to have been transported rearward into the stratiform region, while part of the airflow turned forward again toward the convective updraft. This pattern is consistent with the possibility of hydrometeor recycling between the convective and stratiform regions. Although the radar retrievals do not directly track individual particles, the inferred circulation suggests a physically plausible pathway through which ice particles generated in the convective region could be advected into the stratiform region, partially re-entrained, and subsequently contribute to renewed growth near the leading line. Such a process would help explain the continued expansion of the stratiform area during the mature stage (Fig. 4b) and provides an important framework for interpreting the microphysical results discussed below.

https://doi.org/10.5194/egusphere-2026-1878
Preprint. Discussion started: 26 June 2026


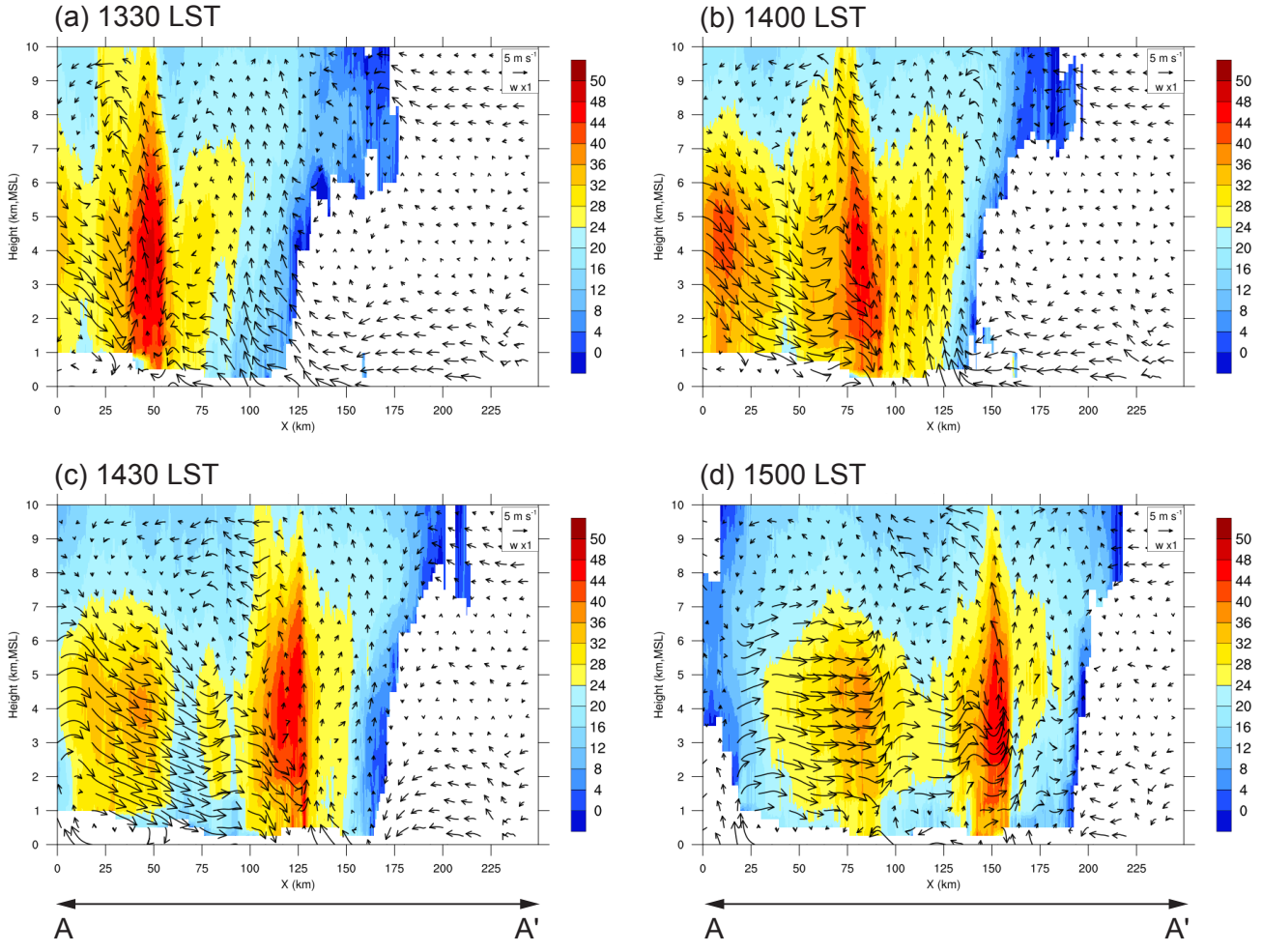


**Figure 6: Vertical cross sections along transect A–A′ in Fig. 5 of reflectivity (dBZ; shading) and winds (m s$^{-1}$; vectors) on 2 August 2020 at (a) 1330, (b) 1400, (c) 1430, and (d) 1500 LST. The reference wind vector is shown in the upper right.**

### 3.2 Microphysical properties of the bow-echo MCS

To examine the microphysical characteristics of the bow-echo MCS during its mature stage, we analyzed radar polarimetric measurements from 1200 to 1600 LST over the domain shown in Fig. 3 (35.5–39.5°N, 123–129°E). The analysis focuses on the contrasts between convective and stratiform regions identified using the echo-classification method, with particular attention to how these differences relate to the kinematic structure described above.

Figure 7 presents contoured frequency by altitude diagrams (CFADs; Yuter and Houze, 1995) for the principal polarimetric variables in the convective and stratiform regions. In the convective region, the CFAD of reflectivity ($Z_H$) exhibits a pronounced peak near 40 dBZ below the melting layer (Fig. 7a), indicating intense precipitation cores associated with strong

https://doi.org/10.5194/egusphere-2026-1878
Preprint. Discussion started: 26 June 2026


updrafts. The relatively coherent vertical distribution of $Z_H$ suggests that the convective cores maintained a vertically organized structure through much of the mature stage, consistent with the deep updrafts seen in the vertical cross sections (Fig. 6).

Below the melting layer, enhanced $Z_{DR}$ values in the convective region indicate the presence of relatively large and oblate raindrops (Fig. 7b). This signature is consistent with active drop growth through collision-coalescence and with size sorting in the convective environment (Dawson et al., 2014; Kumjian and Ryzhkov, 2012). The CFAD of $K_{DP}$ shows a vertically coherent peak near 0.1° $km^{-1}$ and a moderately broad distribution (Fig. 7c), suggesting substantial liquid water content and an abundance of large raindrops. In addition, localized reductions in $\rho_{HV}$ associated with high $Z_H$ (Fig. 7d) indicate the presence of mixed-phase hydrometeors, likely including graupel or hail, within the convective cores. Taken together, these signatures indicate vigorous microphysical growth in the leading line, where strong updrafts, abundant supercooled water, and mixed-phase processes likely acted together to enhance precipitation production.

The trailing stratiform region shows a markedly different polarimetric structure. Its $Z_H$ and $Z_{DR}$ distributions below the melting layer are broader and generally weaker than those in the convective region (Figs. 7e, f), indicating a more heterogeneous raindrop population and weaker local growth rates. The CFAD of $K_{DP}$ peaks near 0° $km^{-1}$ (Fig. 7g), consistent with reduced liquid water content and a greater contribution from nearly spherical ice particles aloft. Below the melting layer, $\rho_{HV}$ becomes more broadly distributed and locally decreases (Fig. 7h), indicating the presence of melting ice particles mixed with raindrops. These characteristics are consistent with a stratiform region dominated by aggregation aloft, melting near the bright band, and evaporation below it.

Importantly, the microphysical signatures of the stratiform region are also consistent with the kinematic evidence of strong interaction between the leading line and the trailing cloud shield. The broad ice-phase and mixed-phase population aloft suggests that the stratiform region was continually supplied with hydrometeors originating from the convective line. At the same time, the airflow pattern inferred from Fig. 6 suggests that part of this hydrometeor population may have been transported forward again toward the leading convective updraft by the upper branch of the rear inflow. Once incorporated into the convective updraft, these particles could act as embryos for further growth through riming and collection. Although this hydrometeor-recycling pathway cannot be observed directly, the combined kinematic and polarimetric evidence supports its plausibility and suggests that it may have contributed to the persistence of heavy rainfall after landfall.

https://doi.org/10.5194/egusphere-2026-1878
Preprint. Discussion started: 26 June 2026


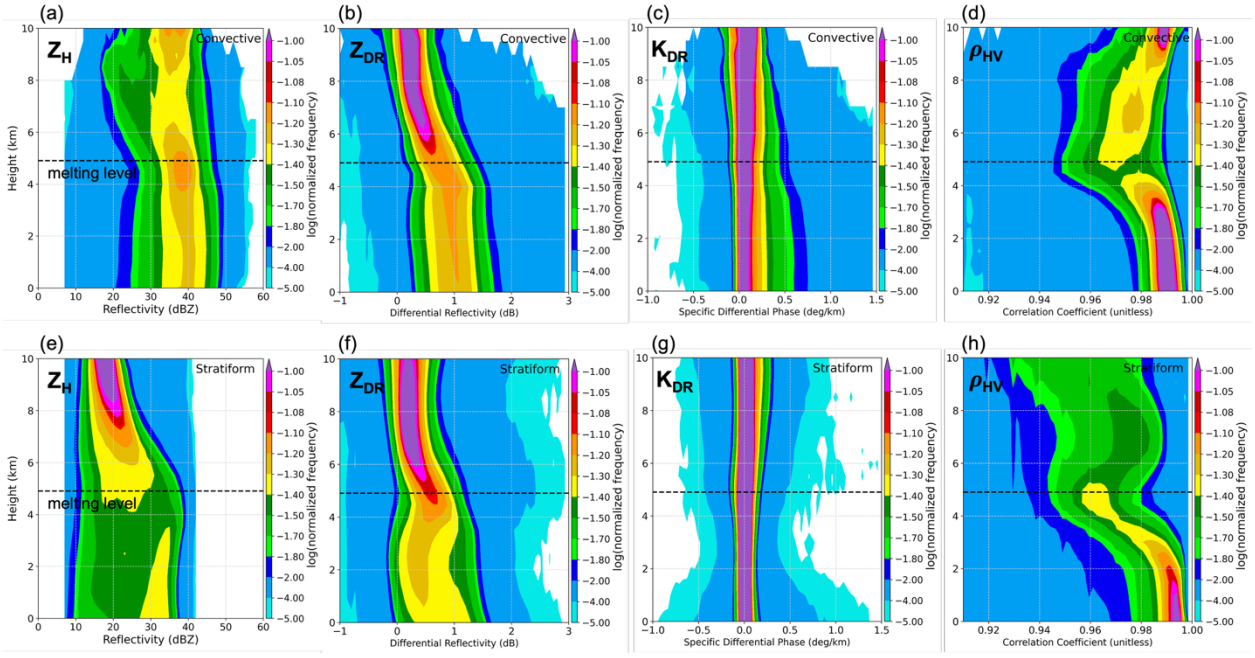


**Figure 7: Contoured frequency by altitude diagrams for convective (top) and stratiform (bottom) regions from 1200 to 1600 LST on 2 August 2020: (a, e) reflectivity (dBZ), (b, f) differential reflectivity (dB), (c, g) specific differential phase (° km^{-1}), and (d, h) correlation coefficient. Data were extracted over 35.5–39.5°N and 123–129°E. The black dashed line indicates the melting-layer height.**

To further examine the vertical variability of microphysical properties, Fig. 8 presents composite profiles of polarimetric and retrieved microphysical variables for the convective and stratiform regions. The convective region exhibits higher median $Z_H$ values and relatively narrow interquartile ranges below the melting layer (Fig. 8a), reflecting concentrated and intense precipitation cores. Higher $Z_{DR}$ values in the convective region (Fig. 8b) indicate larger and more oblate raindrops, consistent with active growth through collision-coalescence, riming, and melting of large ice particles aloft. In both cloud types, $Z_{DR}$ increases toward the surface, indicating continued evolution of the drop-size distribution during descent.

In contrast, stratiform regions show greater variability in $Z_{DR}$ below the melting layer, which suggests a more heterogeneous raindrop population. This broader distribution is consistent with the combined effects of melting, evaporation, weak embedded vertical motions, and possible recirculation of hydrometeors from the convective line. The $K_{DP}$ and $\rho_{HV}$ profiles further distinguish the two regions. Convective regions show a broader $K_{DP}$ distribution (Fig. 8c), indicating greater variability in raindrop concentration and shape, whereas stratiform regions exhibit a narrower distribution more consistent with gradual depositional growth and aggregation. Likewise, the $\rho_{HV}$ distribution in convective regions is relatively narrow, while stratiform regions show a broader range of values below the melting layer (Fig. 8d), reflecting a more complex mixture of melting particles and raindrops.

The retrieved liquid water content (LWC) and ice water content (IWC) further emphasize the contrast between the two regions (Figs. 8e, f). Convective regions exhibit higher and broader distributions of both LWC and IWC, consistent with strong updrafts

https://doi.org/10.5194/egusphere-2026-1878
Preprint. Discussion started: 26 June 2026


that support condensation, riming, and accretion. Above the melting layer, however, the stratiform region shows higher median IWC than the convective region. This result suggests that substantial ice mass was stored aloft within the trailing stratiform cloud, likely as a consequence of rearward transport and aggregation of hydrometeors produced in the convective line. This is an important result because it indicates that a large portion of the storm's ice-phase mass was concentrated not only in the active convective cores but also within the trailing stratiform reservoir.

The retrieved median particle size and total number concentration provide additional evidence of contrasting growth regimes. Convective regions contain larger median particle sizes and broader distributions below the melting layer (Fig. 8g), consistent with rapid growth through riming and collection in a strong-updraft environment. Particle concentrations are also generally higher in the convective region (Fig. 8h), supporting the role of vigorous vertical motions in enhancing hydrometeor production and growth. In the stratiform region, particle sizes are generally smaller and less variable, consistent with slower growth dominated by aggregation and vapor deposition. Nevertheless, occasional larger particles are also present, suggesting that nonlocal transport, partial recycling, and mixed microphysical pathways contributed to the structure of the trailing stratiform cloud.

Overall, the microphysical results complement the kinematic analysis by showing that the leading convective line and trailing stratiform region were dynamically connected but microphysically distinct. The convective region was characterized by strong updraft-supported liquid and mixed-phase growth, whereas the stratiform region served as a broader reservoir of ice-phase hydrometeors and melting precipitation. Together, these features support the interpretation that the persistence and heavy-rainfall efficiency of the bow-echo MCS were closely linked to interactions between storm-scale airflow and evolving hydrometeor populations.

https://doi.org/10.5194/egusphere-2026-1878
Preprint. Discussion started: 26 June 2026


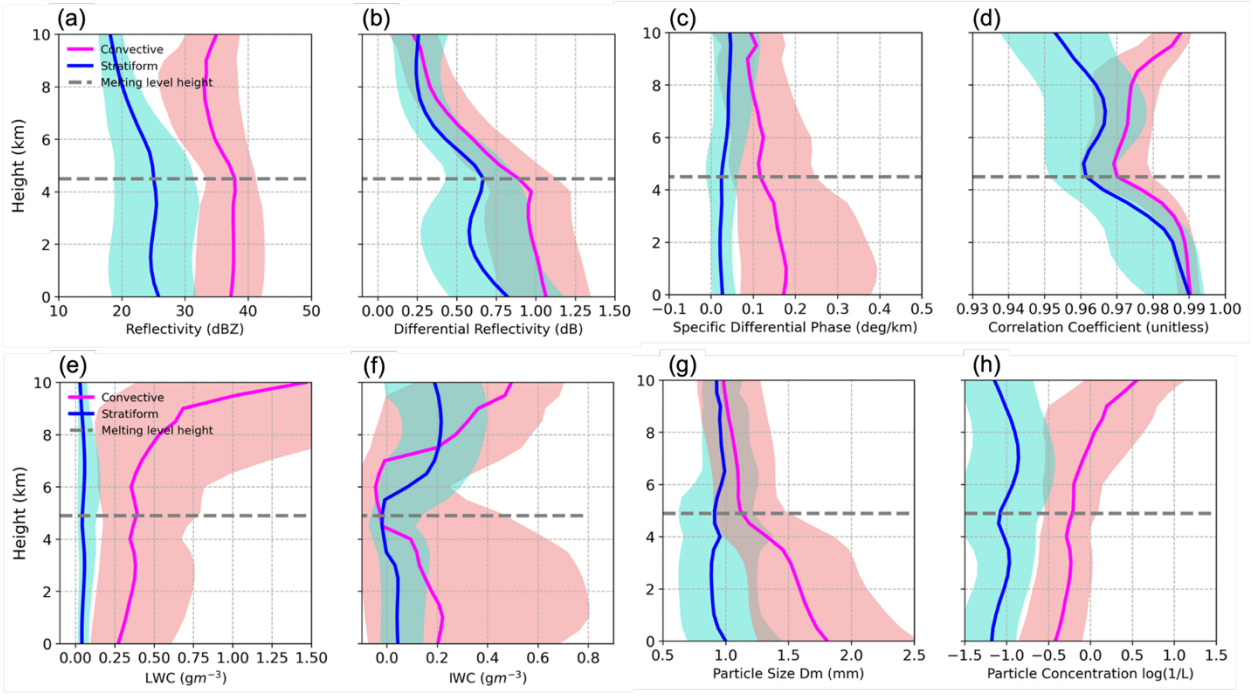


365 **Figure 8: Composite vertical profiles for convective (magenta) and stratiform (blue) regions from 1200 to 1600 LST on 2 August 2020: (a) reflectivity (dBZ), (b) differential reflectivity (dB), (c) specific differential phase (° km$^{-1}$), (d) correlation coefficient, (e) liquid water content (g m$^{-3}$), (f) ice water content (g m$^{-3}$), (g) median particle size (mm), and (h) particle concentration (L$^{-1}$). Data were extracted over 35.5–39.5°N and 123–129°E. Solid lines indicate median values, and shading denotes the interquartile range (25th–75th percentiles). The x-axis in (h) is logarithmic.**

## 370 4 Summary and conclusions

This study presented a detailed analysis of the structural evolution, dynamical processes, and microphysical characteristics of a bow-echo mesoscale convective system (MCS) that developed over the western coast of the Korean Peninsula on 2 August 2020. Using ERA5 reanalysis, multi-Doppler radar wind retrievals, and polarimetric radar observations, we examined the storm's three-dimensional structure during its mature stage, with particular emphasis on the interactions between mesoscale 375 dynamics and microphysical growth processes.

Our analysis showed that the system evolved into a classic leading-convective-line and trailing-stratiform (LCTS) structure. Doppler-derived wind fields revealed a pronounced bowing segment within the leading convective line, enhanced convergence along the leading edge, and asymmetric cyclonic and anticyclonic circulations flanking the bow. These mesoscale circulations contributed to the curvature and maintenance of the bow echo and were associated with localized enhancement of upward 380 motion. A rear-inflow jet (RIJ) developed behind the leading convective line and descended into the trailing stratiform region, where it likely influenced both the thermodynamic structure and the microphysical evolution of the system.

https://doi.org/10.5194/egusphere-2026-1878
Preprint. Discussion started: 26 June 2026


Vertical cross sections showed deep convective updrafts exceeding 5 m $s^{-1}$ and reflectivity cores greater than 40 dBZ, indicating strong convective forcing within the leading line. The presence of a bounded weak echo region (BWER) provided additional evidence of intense vertical motion capable of rapidly lofting hydrometeors. Although the system slowed after landfall, the leading convective line remained coherent for several hours, suggesting that continued interaction between low-level convergence and the descending RIJ helped sustain deep convection during the mature-to-decay transition.

Polarimetric radar analyses revealed clear microphysical contrasts between the convective and stratiform regions. The convective line was characterized by high reflectivity, enhanced $Z_{DR}$, and broader $K_{DP}$ distributions, indicating the presence of large, oblate raindrops and active mixed-phase growth processes, including collision-coalescence, riming, and size sorting. In contrast, the trailing stratiform region exhibited broader and more variable distributions of $Z_H$ and $Z_{DR}$ below the melting layer, consistent with melting, evaporation, aggregation, and a more heterogeneous hydrometeor population. The broader and locally reduced $\rho_{HV}$ values in the stratiform region further support the presence of mixed-phase and melting particles.

The combined kinematic and microphysical analyses suggest an important linkage between storm airflow and hydrometeor evolution. In particular, the retrieved airflow structure is consistent with a hydrometeor-recycling pathway in which particles generated in the leading convective line were transported rearward into the stratiform region and part of that hydrometeor population may subsequently have been redirected toward the convective updraft by the upper branch of the RIJ. Once re-ingested into the convective region, these particles could act as embryos for renewed growth through riming and collection. Although this pathway cannot be directly verified from the radar observations alone, the results provide observational evidence consistent with such a dynamic-microphysical feedback. This process may have contributed to the persistence of strong convection and high precipitation efficiency after landfall.

These findings have important implications for both operational forecasting and numerical modeling. From an operational perspective, the results suggest that the longevity and rainfall intensity of coastal bow echoes may depend not only on the strength of the leading convective line but also on the interaction between the RIJ and the trailing stratiform hydrometeor reservoir. Real-time identification of RIJ intensity, low-level convergence, and stratiform ice extent may therefore help forecasters anticipate the persistence of heavy rainfall and damaging winds in landfalling MCSs. From a modeling perspective, the results highlight the need for numerical weather prediction systems to represent not only cloud microphysical processes but also the mesoscale transport pathways that dynamically connect the convective and stratiform regions of organized convection.

This study is subject to several limitations. First, the analysis focused on a single bow-echo event, and therefore the generality of the inferred processes remains uncertain. Second, although the radar observations provided rich kinematic and microphysical information, the absence of cloud-resolving numerical simulations limits our ability to quantify the detailed thermodynamic forcing and sensitivity to environmental conditions. Future studies should examine additional bow-echo cases over different coastal terrains and under different synoptic environments to determine how robust these processes are. Combining polarimetric radar observations with high-resolution numerical simulations would also help test the proposed

https://doi.org/10.5194/egusphere-2026-1878
Preprint. Discussion started: 26 June 2026


hydrometeor-recycling mechanism more directly and improve understanding and prediction of severe coastal convective systems.

https://doi.org/10.5194/egusphere-2026-1878
Preprint. Discussion started: 26 June 2026


Table 1. The basic information about inputs in WISSDOM

| Platform | Instrument | Location | Sampling (range gate, time interval) |
|---|---|---|---|
| KWK | S-band radar | 126.96, 37.44 | 250 m, 10 mins |
| BRI | S-band radar | 124.63, 37.96 | 250 m, 10 mins |
| KSN | S-band radar | 126.78, 36.01 | 250 m, 10 mins |
| GDK | S-band radar | 127.43, 38.11 | 250 m, 10 mins |
| SAN | C-band radar | 126.49, 36.70 | 250 m, 10 mins |
| IIA | C-band radar | 126.36, 37.46 | 250 m, 10 mins |
| KOU | X-band radar | 127.02, 37.58 | 60 m, 10 mins |
| YOU | X-band radar | 126.93, 37.56 | 60 m, 10 mins |
| DJK | X-band radar | 126.09, 37.25 | 150 m, 10 mins |
| MIL | X-band radar | 126.44, 36.93 | 150 m, 10 mins |
| SRI | X-band radar | 126.90, 37.35 | 150 m, 10 mins |
| Sounding | RS-41 | 126.28, 37.14 | 3-10 m, 6 h |
| LDAPS | Reanalysis data | | 1500 m (horizontal), 0-40000 m by 70 levels 3 h |
| AWS | Surface Stations | | 1 min |

420

https://doi.org/10.5194/egusphere-2026-1878
Preprint. Discussion started: 26 June 2026


## Code, data, or code and data availability

The radar, sounding, radar wind profiler, HSR, WISSDOM and AWS dataset is freely available from the KMA website (https://data.kma.go.kr, last access: 30 March 2026). Please note that the official language of this website is Korean, and more information and assistance can be found in their interface when proceed with the registration (https://data.kma.go.kr/cmmn/selectMemberAgree.do, last access: 30 March 2026). Figures were made with NCL (NCAR Command Language) version 6.2.2 (https://doi.org/10.5065/D6WD3XH5, NCAR, 2019).

## Supplement link

The supplement related to this article is available online.

## Author contributions

This work was made possible by contribution from all authors. Conceptualization, JHJ, SHK, and GWL; methodology, JHJ, SHK, SBO, and CLT; software, JHJ, SHK, SBO, CLT, and JEL; validation, JHJ, SHK,; formal analysis, JHJ, SHK,; investigation, JHJ, SHK, and SBO; writing–original draft preparation, JHJ, SHK, SBO; writing–review and editing, JHJ, SHK, SBO, CLT, GWL, and JEL; visualization, JHJ, CLT, JEL and ; supervision, SHK, GWL; funding acquisition, SHK and GWL. All authors have read and agreed to the published version of the manuscript.

## Competing interests

The contact author has declared that none of the authors has any competing interests.

## Disclaimer

Publisher's note: Copernicus Publications remains neutral with regard to jurisdictional claims made in the text, published maps, institutional affiliations, or any other geographical representation in this paper. While Copernicus Publications makes every effort to include appropriate place names, the final responsibility lies with the authors. Views expressed in the text are those of the authors and do not necessarily reflect the views of the publisher.

## Acknowledgements

The authors would like to thank the participants of the field campaign "Korea Precipitation Observation Program: international collaborative experiments for Mesoscale convective system in Seoul metropolitan area" (KPOP-MS), hosted by the Korea Meteorological Administration (KMA).

https://doi.org/10.5194/egusphere-2026-1878
Preprint. Discussion started: 26 June 2026


**Financial support**

This work was funded by the Korean Meteorological Administration Research and Development Program under Grant RS-2023-00237740.

**References**

Adams-Selin, R. D., van den Heever, S. C., and Johnson, R. H.: Sensitivity of Bow-Echo Simulation to Microphysical Parameterizations, Weather Forecast., 28, 1188–1209, https://doi.org/https://doi.org/10.1175/WAF-D-12-00108.1, 2013.

Brandes, E. A., Zhang, G., and Vivekanandan, J.: Drop Size Distribution Retrieval with Polarimetric Radar: Model and Application, Journal of Applied Meteorology, 43, 461–475, https://doi.org/https://doi.org/10.1175/1520-0450(2004)043<0461:DSDRWP>2.0.CO;2, 2004.

Braun, S. A. and Houze, R. A.: The evolution of the 10–11 June 1985 PRE-STORM squall line: Initiation, development of rear inflow, and dissipation, Mon. Wea. Rev., 125, 478–504, https://doi.org/https://doi.org/10.1175/1520-0493(1997)125<0478:TEOTJP>2.0.CO;2, 1997.

Bryan, G. H. and Morrison, H.: Sensitivity of a simulated squall line to horizontal resolution and parameterization of microphysics, Mon. Wea. Rev., 140, 202–225, 2012.

Carlin, J. T., Reeves, H. D., and Ryzhkov, A. V: Polarimetric Observations and Simulations of Sublimating Snow: Implications for Nowcasting, J. Appl. Meteorol. Climatol., 60, 1035–1054, https://doi.org/https://doi.org/10.1175/JAMC-D-21-0038.1, 2021.

Chen, D., Guo, J., Yao, D., Lin, Y., Zhao, C., Min, M., Xu, H., Liu, L., Huang, X., Chen, T., and Zhai, P.: Mesoscale Convective Systems in the Asian Monsoon Region From Advanced Himawari Imager: Algorithms and Preliminary Results, Journal of Geophysical Research: Atmospheres, 124, 2210–2234, https://doi.org/https://doi.org/10.1029/2018JD029707, 2019.

Chen, H., Xu, W., Liu, N., Sun, J., and Fu, J.: Climatologies of Mesoscale Convective Systems over China Observed by Spaceborne Radars, Mon. Weather Rev., 150, 2697–2717, https://doi.org/https://doi.org/10.1175/MWR-D-22-0002.1, 2022.

Cho, Y.-H., Lee, G. W., Kim, K.-E., and Zawadzki, I.: Identification and Removal of Ground Echoes and Anomalous Propagation Using the Characteristics of Radar Echoes, J. Atmos. Ocean. Technol., 23, 1206–1222, https://doi.org/https://doi.org/10.1175/JTECH1913.1, 2006.

Cifelli, R., Petersen, W. A., Carey, L. D., Rutledge, S. A., and da Silva Dias, M. A. F.: Radar observations of the kinematic, microphysical, and precipitation characteristics of two MCSs in TRMM LBA, Journal of Geophysical Research: Atmospheres, 107, LBA 44-1-LBA 44-16, https://doi.org/https://doi.org/10.1029/2000JD000264, 2002.

Coniglio, M. C., Stensrud, D. J., and Richman, M. B.: An Observational Study of Derecho-Producing Convective Systems, Weather Forecast., 19, 320–337, https://doi.org/https://doi.org/10.1175/1520-0434(2004)019<0320:AOSODC>2.0.CO;2, 2004.

https://doi.org/10.5194/egusphere-2026-1878
Preprint. Discussion started: 26 June 2026


Cui, W., Dong, X., Xi, B., and Feng, Z.: Climatology of linear mesoscale convective system morphology in the United States based on the random-forests method, J. Climate, 34, 7257–7276, 2021.

Churchill D. D., and Houze, R. A.: Development and structure of winter monsoon cloud clusters on 10 December 1978, J. Atmos. Sci., 41, 933–960, 1984.

Dawson, D. T., Mansell, E. R., Jung, Y., Wicker, L. J., Kumjian, M. R., and Xue, M.: Low-Level ZDR Signatures in Supercell Forward Flanks: The Role of Size Sorting and Melting of Hail, J. Atmos. Sci., 71, 276–299, https://doi.org/https://doi.org/10.1175/JAS-D-13-0118.1, 2014.

Gao, J., Xue, M., Shapiro, A., and Droegemeier, K. K.: A Variational Method for the Analysis of Three-Dimensional Wind Fields from Two Doppler Radars, Mon. Weather Rev., 127, 2128–2142, https://doi.org/https://doi.org/10.1175/1520-0493(1999)127<2128:AVMFTA>2.0.CO;2, 1999.

Hersbach, H., Bell, B., Berrisford, P., Hirahara, S., Horányi, A., Muñoz-Sabater, J., Nicolas, J., Peubey, C., Radu, R., Schepers, D., Simmons, A., Soci, C., Abdalla, S., Abellan, X., Balsamo, G., Bechtold, P., Biavati, G., Bidlot, J., Bonavita, M., De Chiara, G., Dahlgren, P., Dee, D., Diamantakis, M., Dragani, R., Flemming, J., Forbes, R., Fuentes, M., Geer, A., Haimberger, L., Healy, S., Hogan, R. J., Hólm, E., Janisková, M., Keeley, S., Laloyaux, P., Lopez, P., Lupu, C., Radnoti, G., de Rosnay, P., Rozum, I., Vamborg, F., Villaume, S., and Thépaut, J.-N.: The ERA5 global reanalysis, Quarterly Journal of the Royal Meteorological Society, 146, 1999–2049, https://doi.org/https://doi.org/10.1002/qj.3803, 2020.

Heymsfield, A. J., Bansemer, A., Heymsfield, G., and Fierro, A. O.: Microphysics of Maritime Tropical Convective Updrafts at Temperatures from −20° to −60°, J. Atmos. Sci., 66, 3530–3562, https://doi.org/https://doi.org/10.1175/2009JAS3107.1, 2009.

Houze Jr., R. A.: Mesoscale convective systems, Reviews of Geophysics, 42, https://doi.org/https://doi.org/10.1029/2004RG000150, 2004.

Houze, R. A.: Observed structure of mesoscale convective systems and implications for large-scale heating, Quart. J. Roy. Meteor. Soc., 115, 425–461, https://doi.org/https://doi.org/10.1002/qj.49711548702, 1989.

Houze, R. A.: Stratiform precipitation in regions of convection: A meteorological paradox?, Bull. Amer. Meteor. Soc., 78, 2179–2196, https://doi.org/https://doi.org/10.1175/1520-0477(1997)078<2179:SPIROC>2.0.CO;2, 1997.

Houze, R. A.: 100 Years of Research on Mesoscale Convective Systems, Meteorological Monographs, 59, 17.1-17.54, https://doi.org/https://doi.org/10.1175/AMSMONOGRAPHS-D-18-0001.1, 2018.

Kumjian, M. R. and Ryzhkov, A. V: The Impact of Size Sorting on the Polarimetric Radar Variables, J. Atmos. Sci., 69, 2042–2060, https://doi.org/https://doi.org/10.1175/JAS-D-11-0125.1, 2012.

Kumjian, M. R., Prat, O. P., Reimel, K. J., van Lier-Walqui, M., and Morrison, H. C.: Dual-Polarization Radar Fingerprints of Precipitation Physics: A Review, Remote Sens. (Basel)., 14, https://doi.org/10.3390/rs14153706, 2022.

Liou, Y.-C. and Chang, Y.-J.: A Variational Multiple–Doppler Radar Three-Dimensional Wind Synthesis Method and Its Impacts on Thermodynamic Retrieval, Mon. Weather Rev., 137, 3992–4010, https://doi.org/https://doi.org/10.1175/2009MWR2980.1, 2009.

https://doi.org/10.5194/egusphere-2026-1878
Preprint. Discussion started: 26 June 2026


Liou, Y.-C., Chang, S.-F., and Sun, J.: An Application of the Immersed Boundary Method for Recovering the Three-Dimensional Wind Fields over Complex Terrain Using Multiple-Doppler Radar Data, Mon. Weather Rev., 140, 1603–1619, https://doi.org/https://doi.org/10.1175/MWR-D-11-00151.1, 2012.

M. I. Biggerstaff and Listemaa, S. A.: An improved scheme for convective/stratiform echo classification using radar reflectivity, J. Appl. Meteor., 39, 2129–2150, 2000.

M. Steiner, Houze, R. A., and Yuter, S. E.: Climatological characterization of three-dimensional storm structure from operational radar and rain gauge data, J. Appl. Meteor., 34, 1978–2007, 1995.

Meng, Z., Zhang, F., Markowski, P., Wu, D., and Zhao, K.: A Modeling Study on the Development of a Bowing Structure and Associated Rear Inflow within a Squall Line over South China, J. Atmos. Sci., 69, 1182–1207, https://doi.org/https://doi.org/10.1175/JAS-D-11-0121.1, 2012.

Morrison, H., Thompson, G., and Tatarskii, V.: Impact of Cloud Microphysics on the Development of Trailing Stratiform Precipitation in a Simulated Squall Line: Comparison of One- and Two-Moment Schemes, Mon. Weather Rev., 137, 991–1007, https://doi.org/https://doi.org/10.1175/2008MWR2556.1, 2009.

Parker, M. D. and Johnson, R. H.: Organizational Modes of Midlatitude Mesoscale Convective Systems, Mon. Weather Rev., 128, 3413–3436, https://doi.org/https://doi.org/10.1175/1520-0493(2001)129<3413:OMOMMC>2.0.CO;2, 2000.

Powell, S. W., Houze Robert A., and Brodzik, S. R.: Rainfall-Type Categorization of Radar Echoes Using Polar Coordinate Reflectivity Data, J. Atmos. Ocean. Technol., 33, 523–538, https://doi.org/https://doi.org/10.1175/JTECH-D-15-0135.1, 2016.

Przybylinski, R. W.: The Bow Echo: Observations, Numerical Simulations, and Severe Weather Detection Methods, Weather Forecast., 10, 203–218, https://doi.org/https://doi.org/10.1175/1520-0434(1995)010<0203:TBEONS>2.0.CO;2, 1995.

R. A., H.: A climatological study of vertical transports by cumulus-scale convection, J. Atmos. Sci., 30, 1112–1123, 1973.

Ray, P. S., Ziegler, C. L., Bumgarner, W., and Serafin, R. J.: Single- and Multiple-Doppler Radar Observations of Tornadic Storms, Mon. Weather Rev., 108, 1607–1625, https://doi.org/https://doi.org/10.1175/1520-0493(1980)108<1607:SAMDRO>2.0.CO;2, 1980.

Rotunno, R., Klemp, J. B., and Weisman, M. L.: A Theory for Strong, Long-Lived Squall Lines, Journal of Atmospheric Sciences, 45, 463–485, https://doi.org/https://doi.org/10.1175/1520-0469(1988)045<0463:ATFSLL>2.0.CO;2, 1988.

Ryzhkov, A. V and Zrnic, D. S.: Discrimination between Rain and Snow with a Polarimetric Radar, Journal of Applied Meteorology, 37, 1228–1240, https://doi.org/https://doi.org/10.1175/1520-0450(1998)037<1228:DBRASW>2.0.CO;2, 1998.

S. E. Yuter and Houze, R. A.: Measurements of raindrop size distributions over the Pacific warm pool and implications for Z–R relations, J. Appl. Meteor., 36, 847–867, 1997.

Smull, B. F. and Houze, R. A.: A Midlatitude Squall Line with a Trailing Region of Stratiform Rain: Radar and Satellite Observations, Mon. Weather Rev., 113, 117–133, https://doi.org/https://doi.org/10.1175/1520-0493(1985)113<0117:AMSLWA>2.0.CO;2, 1985.

https://doi.org/10.5194/egusphere-2026-1878
Preprint. Discussion started: 26 June 2026


SUZUKI, S., MAESAKA, T., IWANAMI, K., SHIMIZU, S., and KIEDA, K.: X-band Dual-Polarization Radar Observations of the Supercell Storm that Generated an F3 Tornado on 6 May 2012 in Ibaraki Prefecture, Japan, Journal of the Meteorological Society of Japan. Ser. II, 96A, 25–33, https://doi.org/10.2151/jmsj.2017-019, 2018.

Tai-Jen Chen, G. and Yu, C.-C.: Study of Low-Level Jet and Extremely Heavy Rainfall over Northern Taiwan in the Mei-Yu Season, Mon. Weather Rev., 116, 884–891, https://doi.org/https://doi.org/10.1175/1520-0493(1988)116<0884:SOLLJA>2.0.CO;2, 1988.

Tao, W.-K., Chen, J.-P., Li, Z., Wang, C., and Zhang, C.: Impact of aerosols on convective clouds and precipitation, Reviews of Geophysics, 50, https://doi.org/https://doi.org/10.1029/2011RG000369, 2012.

Tsai, C.-L., Kim, K., Liou, Y.-C., and Lee, G.: High-resolution 3D winds derived from a modified WISSDOM synthesis scheme using multiple Doppler lidars and observations, Atmos. Meas. Tech., 16, 845–869, https://doi.org/10.5194/amt-16-845-2023, 2023.

Uccellini, L. W. and Johnson, D. R.: The Coupling of Upper and Lower Tropospheric Jet Streaks and Implications for the Development of Severe Convective Storms, Mon. Weather Rev., 107, 682–703, https://doi.org/https://doi.org/10.1175/1520-0493(1979)107<0682:TCOUAL>2.0.CO;2, 1979.

Wakimoto, R. M.: Convectively Driven High Wind Events, Meteorological Monographs, 28, 255–298, https://doi.org/https://doi.org/10.1175/0065-9401-28.50.255, 2001.

Weisman, M. L.: The Role of Convectively Generated Rear-Inflow Jets in the Evolution of Long-Lived Mesoconvective Systems, Journal of Atmospheric Sciences, 49, 1826–1847, https://doi.org/https://doi.org/10.1175/1520-0469(1992)049<1826:TROCGR>2.0.CO;2, 1992.

Weisman, M. L.: The Genesis of Severe, Long-Lived Bow Echoes, Journal of Atmospheric Sciences, 50, 645–670, https://doi.org/https://doi.org/10.1175/1520-0469(1993)050<0645:TGOSLL>2.0.CO;2, 1993.

Ye, B.-Y., Lee, G., and Park, H.-M.: Identification and removal of non-meteorological echoes in dual-polarization radar data based on a fuzzy logic algorithm, Adv. Atmos. Sci., 32, 1217–1230, https://doi.org/10.1007/s00376-015-4092-0, 2015.

Yuter, S. E. and Houze, R. A.: Three-Dimensional Kinematic and Microphysical Evolution of Florida Cumulonimbus. Part II: Frequency Distributions of Vertical Velocity, Reflectivity, and Differential Reflectivity, Mon. Weather Rev., 123, 1941–1963, https://doi.org/https://doi.org/10.1175/1520-0493(1995)123<1941:TDKAME>2.0.CO;2, 1995.